



Effects of Mo content on the microstructure and mechanical properties of laser cladded FeCoCrNiMo_x ($x = 0.2, 0.5$) high-entropy alloy coatings

Junjun Jin ^a, Bing Chen ^a, Zhiyi Zhang ^b, Yibin Wu ^c, Zhaoyang Luo ^c, Guoqing Gou ^{a,*}, Wenjing Chen ^{c,*}

^a Key Laboratory of Advanced Technologies of Materials, Ministry of Education, School of Materials Science and Engineering, Southwest Jiaotong University, Chengdu 610031, China

^b CRRC QINGDAO SIFANG CO., LTD, Qingdao 266111, China

^c School of Materials Science and Engineering, Xihua University, Chengdu 610039, China



ARTICLE INFO

Keywords:

Laser cladding

High entropy alloy coatings

Impact toughness

Microstructure

First principles calculations

ABSTRACT

The laser cladding additive manufacturing technology and high-entropy alloys can serve as ideal techniques and materials for the surface repair of high-speed train axles. Coatings of FeCoCrNiMo_x ($x = 0.2, 0.5$) were prepared on EA4T axle steel using laser cladding technology, and their phase, structure, and mechanical properties were analyzed using X-ray diffraction (XRD), electron backscatter diffraction (EBSD) and electron channeling contrast imaging (ECCI) characterization techniques. Additionally, the mechanical properties of the coatings were tested, and first-principles calculations were used to verify and calculate the material's mechanical performance. The research findings indicate that an increase in Mo content leads to a greater degree of lattice distortion, causing a leftward shift in diffraction peak positions. Significant differences in the microstructure from the substrate to the coating surface were observed, with columnar grain structure at the bottom of the cladding layer and equiaxed dendrites dominating the coating surface. The increase in Mo content promotes the formation of σ phase while also refining the grain size. ECCI results show that both types of coatings consist of a high-density dislocation cell structure and Mo-rich particles. With an increase in Mo content, the peak hardness of the coating increased from 456.5 HV to 469.4 HV, while the impact energy decreased from 56 J to 16 J, attributed to the increase in dislocation density and the greater quantity of σ phase. First principles calculations verified that the comprehensive mechanical properties of FeCoCrNiMo_{0.2} are superior, providing theoretical guidance for the optimization and design of the coatings.

1. Introduction

Since the operation of the first Shinkansen in Japan in the 1970s, high-speed trains have undergone rapid development over half a century. The technology of high-speed trains has strongly supported the development of the world economy and the progress of civilization. The axle serves as a crucial component of the train, bearing various loads from the body and track, as well as operating in complex and changing environments [1]. They constitute the main causes of axle failure. Currently, the conventional approach to dealing with failed axles is direct scrapping, resulting in not only incurs high costs but also poses significant environmental hazards. In the context of low-carbon technology and a low-carbon economy, how to achieve the repair of failed axles on the basis of safety and reliability, thereby extending the service

life of axles, becomes one of the core scientific issues in mechanical structure remanufacturing engineering [2–5]. The application of high entropy alloy coating is of great significance in the repair and protection of high-speed train axles. High entropy alloy is a homogeneous solid solution composed of five or more elements, and its unique microstructure and excellent properties make it an ideal coating material. Laser cladding technology can evenly cover the high entropy alloy coating on the surface of the axle, forming a strong protective layer, and can meet the requirements of axle impact resistance.

To remanufacture damaged axles and restore them to their original size and function, conventional process methods include argon arc welding, plasma spraying, vacuum brazing, and other repair technologies [6–8]. However, these surface repair technologies have some unavoidable drawbacks, such as thin thickness, poor density, and low

* Corresponding authors at: 111, Section 1, North Second Ring Road, Chengdu 610031, China.

E-mail addresses: gouguoqing1001@163.com (G. Gou), njchenwenjing@163.com (W. Chen).

Table 1

Main chemical composition of EA4T steel (wt%).

C	Si	Mn	P	S	Cr	Ni	Mo	Cu	Fe
0.257	0.344	0.748	0.008	0.002	1.039	0.257	0.246	0.151	bal

Table 2

Mechanical properties of EA4T steel.

Tensile strength Rm/MPa	Yield strength Re/MPa	Elongation δ/%	Impact energy J(20 °C)
650–800	≥420	≥18	≥50

bonding strength with the substrate. In response to the problems existing in the repair manufacturing process mentioned above, the advantages of laser cladding as a remanufacturing technology are manifested. It has the advantages of low heat input, high energy concentration, high surface uniformity, high deposition rate, and low substrate dilution, and is widely used in axle repair [9–12]. At the same time, laser cladding is a coating preparation technology that uses a defocused laser beam to melt pre-placed or synchronously fed powder/wire. The diversity of cladding materials also makes its application range wider [13,14]. Although laser cladding coatings can bring positive effects, the cladding metal faces high crack sensitivity and poor processing performance, which greatly limits the structural performance of the cladding layer and structure [15]. Therefore, the design and selection of cladding materials are crucial [16–18].

High entropy alloys (HEAs) are increasingly important in materials science, particularly in the development of coatings for surface repair. High-entropy alloys, compared to traditional nickel-based and iron-based alloys, feature a uniform distribution of multiple elements, exhibiting excellent high-temperature stability and oxidation resistance. They also demonstrate outstanding strength and toughness, maintaining good mechanical properties at both high and low temperatures. Additionally, they possess good wear resistance and corrosion resistance. The surface coatings manufactured by laser cladding technology have the characteristics of high bonding strength, dense structure, good surface forming effect, and low dilution rate. Traditional high entropy alloy system tend to form complex intermetallic compounds, which have adverse effects on the comprehensive performance of the alloy. In alloy design, density functional theory (DFT) can be used to calculate the lattice constants of different composition alloys in the first principle to determine the most stable lattice structure. By adjusting the ratio of different elements, the lattice constants of the alloy can be optimized, which affects the stability and properties of the alloy. At the same time, the formation energy of the alloy with different composition is predicted, so as to evaluate the stability of the alloy. By comparing the formation energies of alloys with different compositions, the appropriate element composition can be selected to avoid the formation of unfavorable intermetallic compounds, thus improving the overall properties of the alloy. Therefore, Yeh et al. [19–23] proposed the concept of multi-component HEAs, which provides a new approach for the development and design of new cladding materials. Since then, starting with the five-component alloy of CrMnFeCoNi and other elements, a new era of multi-component alloy design has been opened. Through this calculation method, we were able to gain a deep understanding of the mechanical properties of different coating components, thus providing important theoretical support for our research results [24–27]. FeCoCrNiMo belongs to the category of high entropy alloy, and the existing literature shows that it has excellent mechanical properties, corrosion resistance and high temperature stability, but there is a lack of in-depth research on laser cladding process molding. Studying the behavior of this particular alloy system under laser cladding conditions may provide valuable insights into its response, microstructure evolution, and resulting mechanical properties during hot working. The

FeCoCrNiMo alloy system provides a combination of different elements that can be adjusted to achieve specific properties by adjusting trace elements. The presence of multiple elements makes it possible to obtain a variety of microstructures and phase compositions that can be optimized to obtain the desired mechanical and physical properties. This flexibility in performance customization makes the FeCoCrNiMo system an interesting research and development object in the field of advanced materials.

In this study, Mo-doped HEAs coatings are prepared by laser cladding technology, and the influence of Mo element on the microstructure, hardness, and impact resistance of HEAs coatings is investigated through first-principles calculations, laser surface cladding technology, and advanced characterization techniques. This provides experimental data and theoretical basis for understanding the microstructure and mechanical properties of HEAs, and has important guiding significance for the development of new high entropy alloy materials. Our research results contribute to expanding the application field of HEAs and provide reference for the alloy design of related materials.

2. Materials and methods

2.1. HEAs coating preparation

The EA4T axle steel with dimensions of $160 \times 160 \times 12$ mm is used as the substrate in this study. The main chemical composition is shown in Table 1. The supply state of the EA4T axle steel is quenched and tempered, and its microstructure mainly consists of tempered martensite and a small amount of blocky ferrite. The mechanical properties are shown in Table 2. The cladding material is FeCoCrNiMo_x ($x = 0.2, 0.5$) powder, prepared by vacuum atomization, and its chemical composition is shown in Fig. 1 (a, b). The chemical composition is given as a percentage of atoms, indicating the relative amount of each element in the alloy. Before the cladding test, the powder needed to be dried at 120 °C in a vacuum oven for 2 h to improve its flowability. Fig. 1 (c) shows the main equipment for the laser cladding test, which consists of a water chiller, a 4 kW laser, a computer programming system, an FPHF-20 synchronous powder feeding system, and a four-axis CNC platform. It is operated by the X, Y, and Z axes simultaneously, with a working area of up to 1.2×0.8 m. The cladding length, scanning speed, and other cladding process parameters were controlled through the computer programming system.

Based on the previous work experience of the research group, the laser cladding parameters shown in Table 3 is used to prepare the coatings [28]. The macroscopic surface morphology and cross-sectional morphology of the prepared coatings are shown in Fig. 1 (d). The geometric dimensions and dilution rate of the laser cladding coatings are important references for judging the quality of the coatings. In the measurement of the geometric dimensions of the cladding layer, the cross-section of the cladding layer is magnified using a stereomicroscope (magnification of 14 times), and the cladding width (W), cladding layer height (H), and cladding depth (h) are measured and calculated for the geometric dimensions and dilution rate of the cladding layer [29,30], as shown in Fig. 1 (e). The dilution rate refers to the diffusion of alloying elements from the substrate into the cladding layer due to the melting of the substrate during the laser cladding process. This diffusion results in an increase in the element concentration in the cladding layer and a decrease in the substrate, leading to dilution of the element concentration in the cladding layer. Therefore, the dilution rate is a key indicator of the micro-quality of the cladding layer. The magnitude of the dilution rate reflects the influence of process parameters on the forming quality

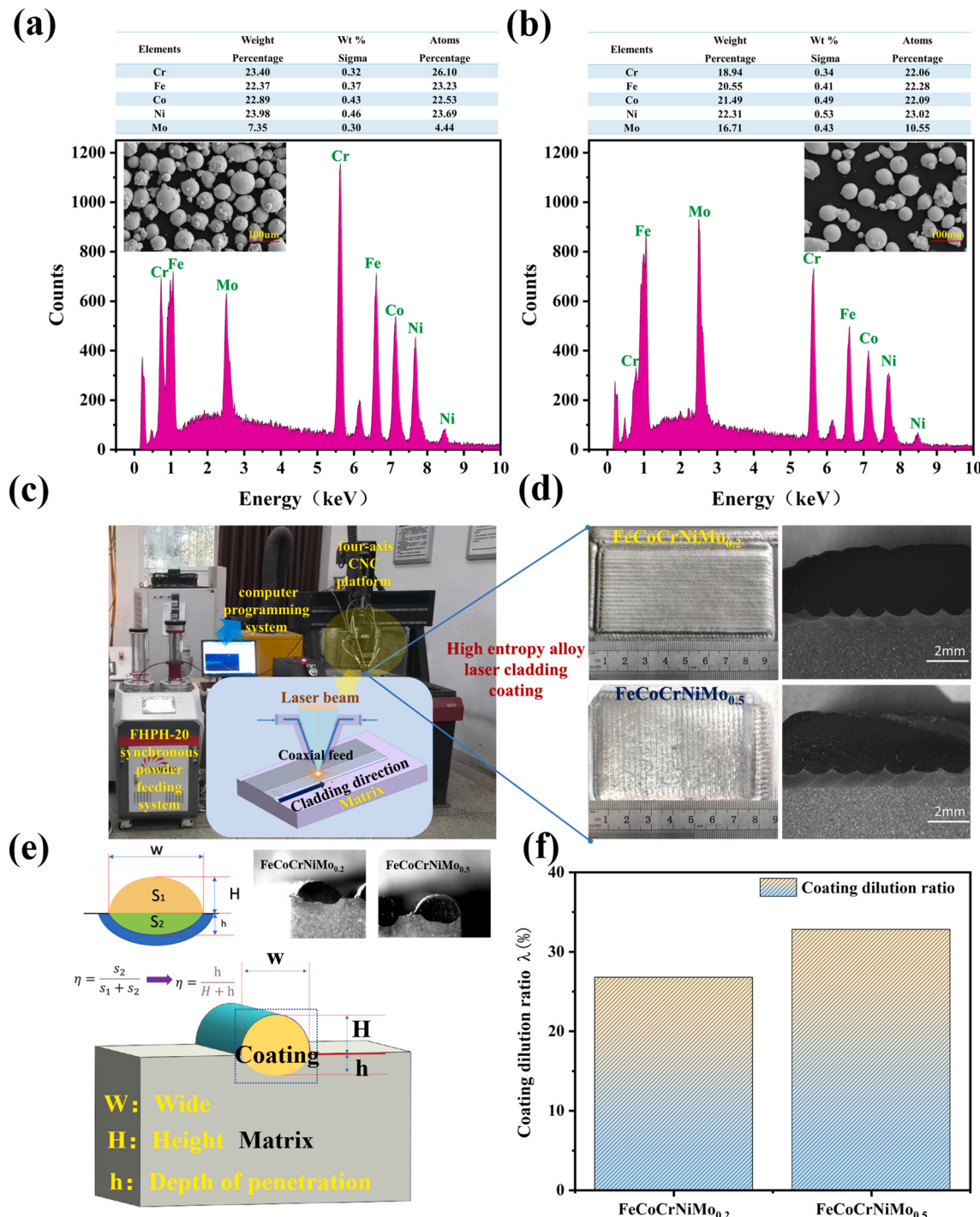


Fig. 1. Preparation of laser cladding HEA coating: (a) FeCoCrNiMo_{0.2} composition; (b) FeCoCrNiMo_{0.5} composition; (c) Schematic diagram of laser cladding equipment and cladding for synchronous powder feeding ; (d) Macroscopic morphology of the surface and cross section of the two coatings ; (e) Schematic diagram of geometric size measurement and dilutions calculation; (f) Dilutions calculation results.

Table 3

Process parameters for fabricating FeCoCrNiMo_x ($x = 0.2, 0.5$) coating by laser cladding.

Laser power/W	Laser type	Wavelength/nm	Powder feeding speed(r/min)	Spot diameter/mm	Speed of scanning(mm/min)	Energy density J/mm ²
2100	Fiber laser	1071	2	5	300	4.12×10^4

to some extent. Generally, the dilution rate is calculated based on the area enclosed by the cladding layer, but the cross-sectional morphology of the cladding layer is often irregular, which introduces significant

errors in the dilution rate calculation. The calculated results of the dilution rate for the two-component coatings are shown in Fig. 1 (f) [31,32]. The results show that the two-component coatings have good

Table 4

Equipment parameters of X-ray diffractometer.

Type of equipment	Target material	Wavelength of wave λ / nm	Tube voltage / KV	Tube current / mA	Angle of scan /°	Scanning speed (°/s)
DX-2500	Cu	100	30	20	20° ~ 100°	0.03

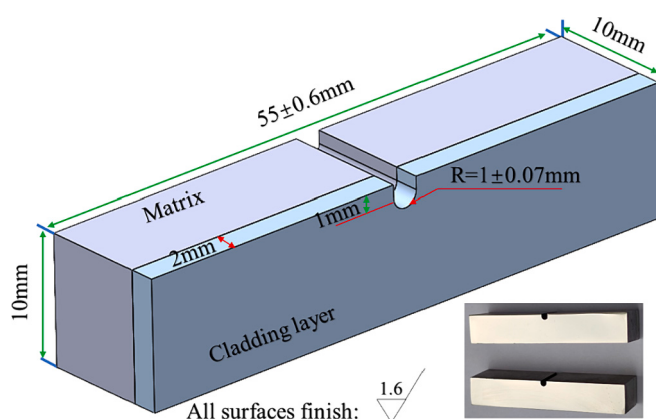
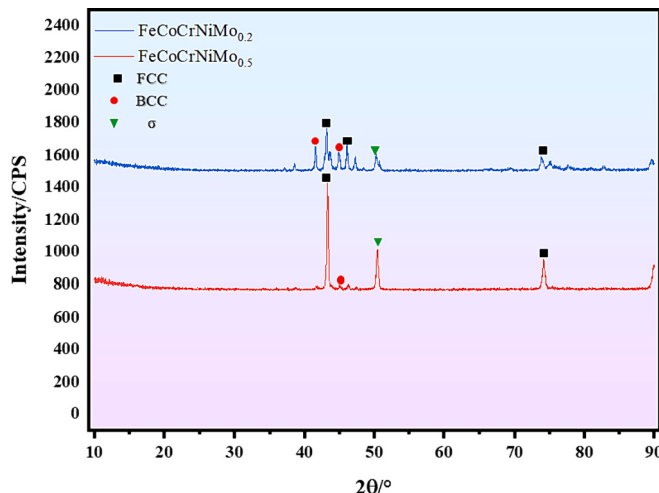


Fig. 2. Specific dimensions of impact samples for coatings.

Fig. 3. X-ray diffraction results of FeCoCrNiMo_x ($x = 0.2, 0.5$) high entropy alloy coating.

formability and moderate dilution rates, similar to other coatings [33].

2.2. Materials characterization

Linear cutting was used to sample the cladding direction perpendicular to the cladding layer. The size of XRD samples was $10 \times 10 \times 15$ mm, and the detection parameters are shown in Table 4. The test results are analyzed by Jade6 software, and PDF-2004 data base was used for phase retrieval. The specific dimensions of the microstructure specimens were $10 \times 8 \times 8$ mm. The specimens were ground by SiC paper from 400 to 5000 grit, polished with $1 \mu\text{m}$ diamond powder. Then, the sample was cleaned by ultrasonic wave and etched with 4 vol% nitric acid-alcohol solution. Finally, electron backscatter diffraction (EBSD) and electron channeling contrast imaging (ECCI) were used to analyze the microstructure of the cladding layer, binding zone, heat affected zone and matrix of the sample. At the same time, energy dispersive spectrometer (EDS) was used to analyze the composition distribution of the sample.

2.3. Mechanical properties

In this paper, JMHVS-1000AT digital microhardness tester was used to test the microhardness of coating and matrix. The specific test parameters were as follows: the loading force was 1.961 N, the holding time was 20s, the spacing between the measurement points was 1 mm, and the test direction was from the four test lines of cladding layer, bonding line, heat affected zone and matrix. In order to more intuitively show the hardness changes in different areas of the cladding sample, we selected 30 different points of equal distance in the horizontal position of each test line. In addition, a U-notch impact specimen and a JB-300B pendulum impact testing machine were used to evaluate the impact bearing capacity of the coating. The impact test was carried out according to the standard: Standardization Administration of the People's Republic of China. GB/T229-2020, Standard for Charpy pendulum impact test methods for metallic materials [34]. The specific size of the impact sample of the coating is shown in Fig. 2.

2.4. First principles calculations

First principles calculations are a computational method based on the principles of quantum mechanics, which can be used to study the electronic structure and mechanical properties of metallic materials. By solving the Schrödinger equation, we can accurately predict the mechanical performance of materials without relying on experimental data or empirical parameters. This provides important theoretical guidance for material design and performance optimization.

We employed first-principles numerical simulations based on density functional theory by performing first-principles calculations using the Cambridge Sequence Total Energy Package (CASTEP) together with the Perdew-Burke-Ernzerh (PBE) Generalized Gradient Approximate (GGA) calculation of the exchange correlation function for a plane wave cutoff energy of 420 eV [33]. A grid of k-points spaced 0.04 Å apart was sampled according to the Monkhorst-Pack method of the Brillouin zone. The Pauli exclusion criterion was used for density mixing schemes for self-consistent fields, with the error to 1×10^{-6} eV/atom. In the ATAT (Alloy Theoretic Automated Toolkit) alloy theory automation toolkit, the "mcsqs" code is used to generate special quasi-random structure (SQS) models, and the FeCoCrNiMo_x ($x = 0.2, 0.5$) SQS supercell model is used as the basis for geometric optimization. The elastic stiffness constants C_{ij} , bulk modulus B, shear modulus G, Young's modulus E, Poisson's ratio v, and the elastic anisotropy of the structure were obtained for the high entropy alloy in the equilibrium volume structure state.

3. Results and discussion

3.1. Microstructure

Fig. 3 shows the X-ray diffraction spectra of FeCoCrNiMo_x ($x = 0.2, 0.5$) high entropy alloy coatings with different Mo contents. The analysis shows that with an increase in Mo content to 0.5, there is an increase in the intensity of the σ phase diffraction peaks, indicating that Mo facilitates the formation of the σ phase. In addition, the σ phase is composed of intermetallic compounds such as Co_2Mo_3 , CoMo_2Ni , $\text{Cr}_9\text{Mo}_{21}\text{Ni}_{20}$ [35]. Other studies have also shown that the coating of CoCrFeNi high entropy alloy (HEA) with Mo also forms σ phase [36]. The formation mechanism of σ phase can be attributed to the segregation of Mo and Cr elements promoted by Mo elements [37]. This is because the mixing enthalpy of Mo with other alloying elements is relatively small, and Mo

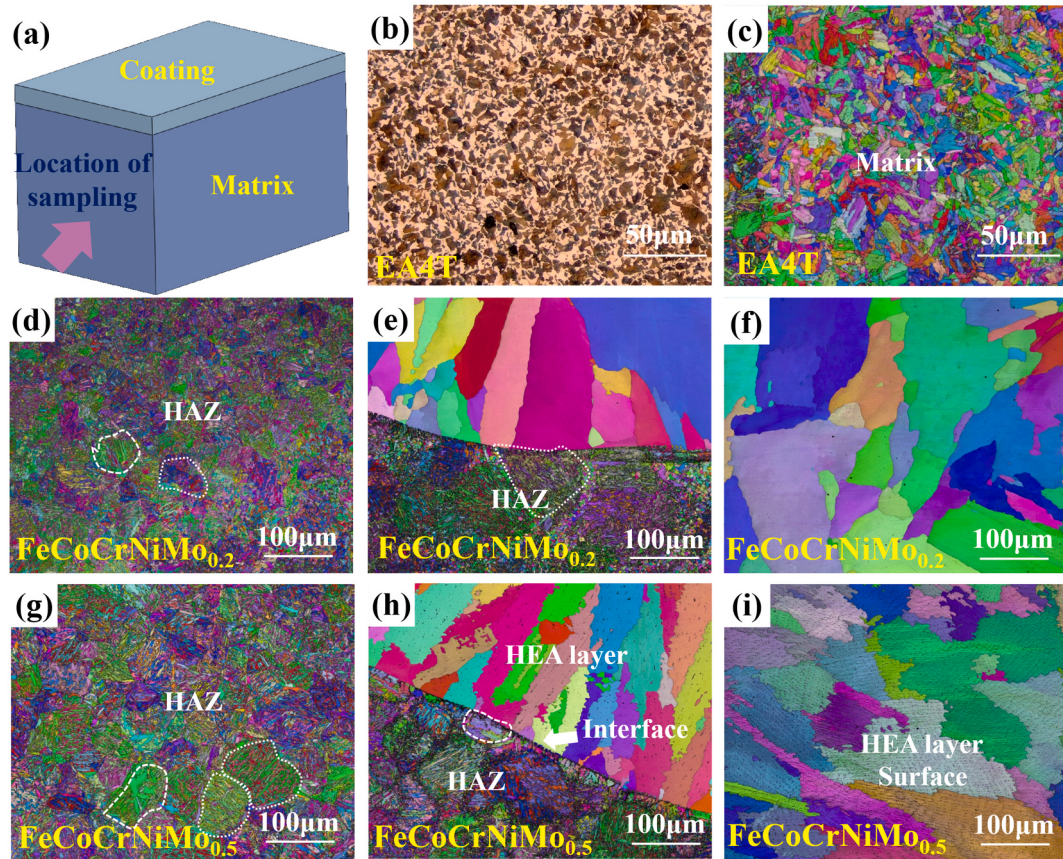


Fig. 4. Microstructure of FeCoCrNiMo_x ($x = 0.2, 0.5$) HEAs coatings and substrate: (a) Schematic diagram of the observation position; (b) Microstructure schematic diagram of EA4T axle steel; (c) Matrix EA4T-EBSD-IPF image; (d, e, f) EBSD-IPF images of $\text{FeCoCrNiMo}_{0.2}$ HEAs coating; (g, h, i) EBSD-IPF images of $\text{FeCoCrNiMo}_{0.5}$ HEAs coating.

easily combines with other elements. As the Mo content increases from 0.2 to 0.5, the tendency to form intermetallic compounds increases [37]. At the same time, as the Mo content increases, the lattice constants of the solid solution phase also gradually increase. The addition of Mo in other HEAs systems can lead to severe lattice distortion of the alloy and promote the formation of intermetallic phases in a similar mechanism [38].

Fig. 4 shows the EBSD characteristic morphology of the microstructure of FeCoCrNiMo_x ($x = 0.2, 0.5$) HEAs coatings. Fig. 4 (a) is a schematic diagram of the observation position. Figs. 4 (b, c) show that the matrix of both components consists of small plate-like martensite, indicating a higher content of ferrite. Figs. 4 (e) (h) show that the boundaries between the two components are very clear, which is due to the differences in composition between the cladding layer and the substrate. Figs. 4 (d) (g) show that the heat-affected zone retains its original microstructure, but the grain size increases under the effect of thermal cycling. Figs. 4 (f) (i) show that the microstructure at the bottom of the two-component cladding layer is mainly columnar crystals, which gradually transition from columnar crystals to equiaxed crystals in the middle of the coating, while the surface of the coating is distributed with equiaxed dendritic crystals. The grain size decreases with increasing Mo content. Related studies show that the interface between laser cladding high entropy alloy coating and substrate is clear. Laser cladding HEA coating is basically composed of three different regions, namely, planar crystal region, columnar crystal region and equiaxed crystal region. This typical crystal morphology is relatively typical in laser cladding coatings. The difference is that with the adjustment of composition, there are differences in grain size, which leads to differences in coating performance [38].

Fig. 5 and Fig. 6 shows the ECCI and EDS features of the microstructure of the FeCoCrNiMo_x ($x = 0.2, 0.5$) coating prepared by laser

cladding. ECCI refers to “Electron Channeling Contrast Imaging” and EDS refers to “Energy Dispersive X-ray Spectroscopy”. ECCI reveals the details of the substructure. As shown in Fig. 5 (a) and Fig. 6 (a), it is found that the coating structure consists of a group of cellular structures [39,40]. It can be seen that the cell walls are decorated with high-density dislocations and some dislocation-related white particles, and these cellular structures are closely arranged to form a honeycomb-like structure. However, the white particles of $\text{FeCoCrNiMo}_{0.5}$ divide a larger area. Figs. 5 (b) (c) show individual dislocations inside the cellular structure. The average size of the cells is about 1500 nm. Figs. 6 (b) (c) clearly show that dislocations are present inside the cellular structure, and these dislocations are intertwined and distributed along the cell walls with the white particles. The average size of the cells is about 1200 nm. Through Energy-dispersive X-ray spectroscopy (EDS) analysis (Fig. 5 (d,e,f,g,h,i) and Fig. 6 (d,e,f,g,h,i), respectively correspond to Fig. 5 (a) and Fig. 6(a)) and related literature, it is confirmed that the white particles are Mo-enriched σ phase, which is distributed along the cell walls in the grain boundaries and within the grains [41–43]. It is also found that there are some black oxides, and the composition of these oxides is Cr_2O_3 , which is caused by the ablation during the laser cladding process. It can be clearly seen that the ablation phenomenon is more severe at the grain boundaries.

By comparing Figs. 5 and 6, it can be observed that the distribution of Mo-enriched intermetallic compounds in the grain boundaries and within the grains is more extensive in the $\text{FeCoCrNiMo}_{0.5}$ HEAs composition. The density of dislocations on the inner walls of the cellular structure is higher, which is also the reason for the increased hardness with the increase of Mo content. Moreover, from the distribution of the oxide Cr_2O_3 , it can be seen that the degree of oxidation is more severe in the $\text{FeCoCrNiMo}_{0.5}$ HEAs composition. Studies have

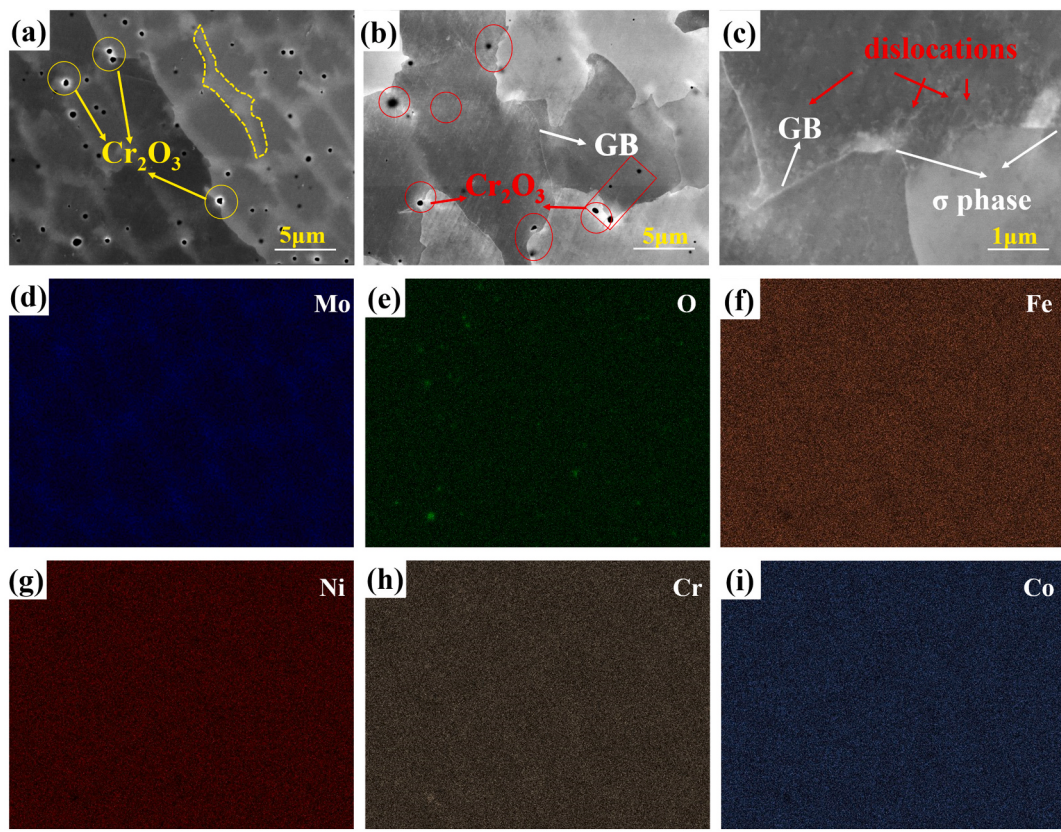


Fig. 5. Microstructure of substrate and coating by FeCoCrNiMo_{0.2} laser cladding: (a) honeycomb low-magnification ECC image; (b)(c) Details of the honeycomb structure; (d)(e)(f)(g)(h)(i) EDS analysis of element distribution.

shown that Mo and Cr elements can precipitate along grain boundaries to form a large number of small size precipitated phases, and the main precipitated phase is σ phase, and the mass fraction of Cr and Mo reaches 35 % and 16 % respectively [44].

3.2. Microhardness

The microhardness distribution of the cross-section of the FeCoCrNiMo_x ($x = 0.2, 0.5$) high-alloy coatings is shown in Fig. 7. From the substrate to the cladding layer, the hardness gradually increases, showing a pronounced gradient. The width of the heat-affected zone is not very large, and the hardness in this region is slightly higher than that of the substrate. From the microhardness distribution maps of the substrate, cladding layer, and heat-affected zone, it can be seen that the hardness of the EA4T steel substrate maintains the properties of the raw material, with an average hardness of 223.8 HV. The average microhardness of the heat-affected zone is 353.8 HV (FeCoCrNiMo_{0.2}) and 360.7 HV (FeCoCrNiMo_{0.5}). The average microhardness of the cladding layer is 424.0 HV (FeCoCrNiMo_{0.2}) and 455.7 HV (FeCoCrNiMo_{0.5}). Compared to the substrate, the microhardness of the heat-affected zone is mainly related to the formation of plate-like martensite due to thermal cycling, but the presence of a small amount of retained austenite also contributes to the increased hardness compared to the substrate. After laser cladding, it can be observed through microscopic observation and XRD analysis that many precipitates (such as Cr₂Mo₃) have formed in the cladding layer in addition to the substrate. During the crystallization process of the cladding layer, a large number of solute atoms can hinder dislocation movement, leading to dislocation pile-up and an intensified solid solution strengthening, resulting in a high-strength and high-hardness solid. The hardness is increased. This phenomenon was also found in the CrCoNiMox alloy, with the addition of Mo element, the hardness of the alloy increased significantly and the plasticity decreased.

Because the intermetallic compounds are hard and brittle, and there is competition between the solution strengthening of Mo and the embrittlement of intermetallic compounds [45,46].

The results show that the microhardness of the FeCoCrNiMo_{0.5} cladding layer is significantly increased, reaching a maximum of 469.4 HV. The FeCoCrNiMo_{0.5} alloy coating has a high hardness, which is the result of the combined effect of multiple factors. Among them, the larger atomic radius of the Mo element causes lattice distortion in the solid solution, increasing the lattice strain energy and thus improving the hardness of the coating. Additionally, the main reason is the formation of more σ phase in the FeCoCrNiMo_{0.5} alloy cladding layer. The σ phase is a metallic intermetallic compound with a tetragonal structure, which has limited slip systems and high hardness. Therefore, an increased content of σ phase in the coating significantly increases the microhardness. Other factors such as grain refinement and interface strengthening also contribute to the hardness of the coating.

3.3. Toughness of impact

The impact test results show that the average impact energy of FeCoCrNiMo_{0.2} is 56 J, while that of FeCoCrNiMo_{0.5} is 16 J, indicating that FeCoCrNiMo_{0.2} has much higher impact toughness than FeCoCrNiMo_{0.5} [47].

The analysis of impact fracture surfaces of laser-cladded coatings of high-entropy alloys can reveal their mechanical properties and fracture characteristics. During the impact test, high-speed impact loads cause plastic deformation and fracture failure of the samples, resulting in different types of fracture surfaces. By analyzing the morphology, size, and shape of the fracture surfaces, the deformation and fracture mechanisms of the materials under impact load can be understood. Figs. 8 (a) and 10 (a) show the macroscopic morphology of the fracture surfaces of the two different compositions of alloy impact samples. It can be

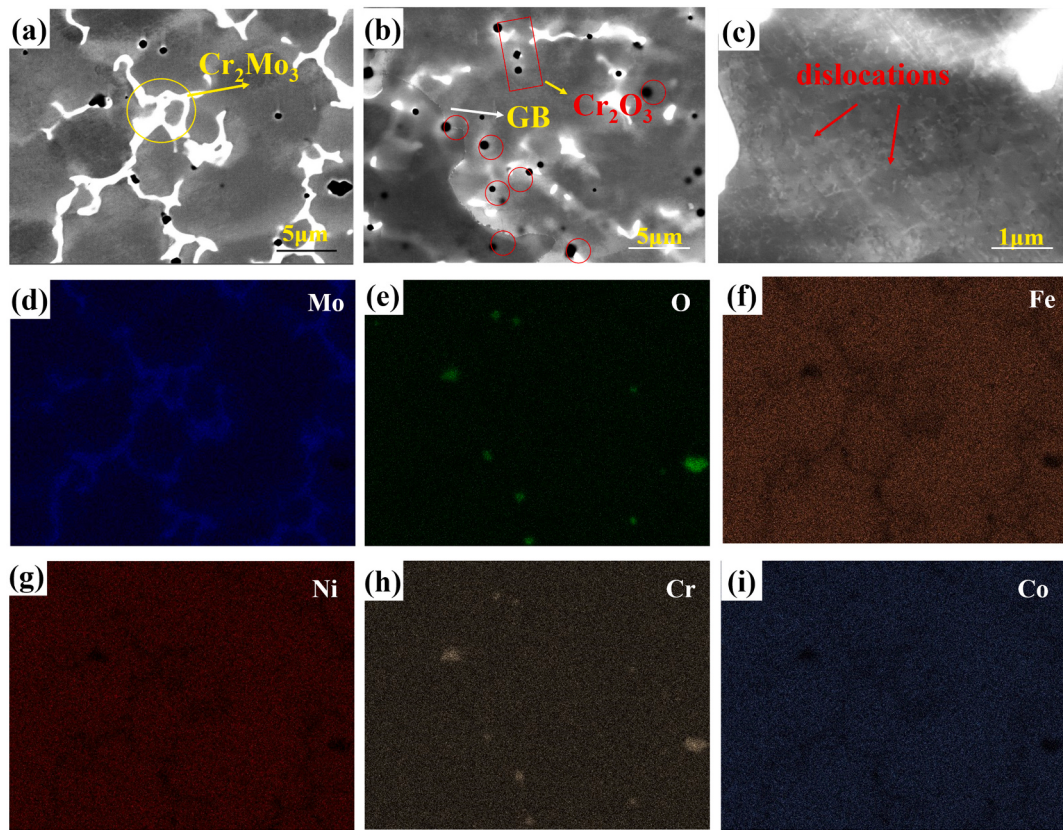


Fig. 6. Microstructure of substrate and coating by FeCoCrNiMo_{0.5} laser cladding: (a) honeycomb low-magnification ECC image; (b)(c) Details of the honeycomb structure; (d)(e)(f)(g)(h)(i) EDS analysis of element distribution.

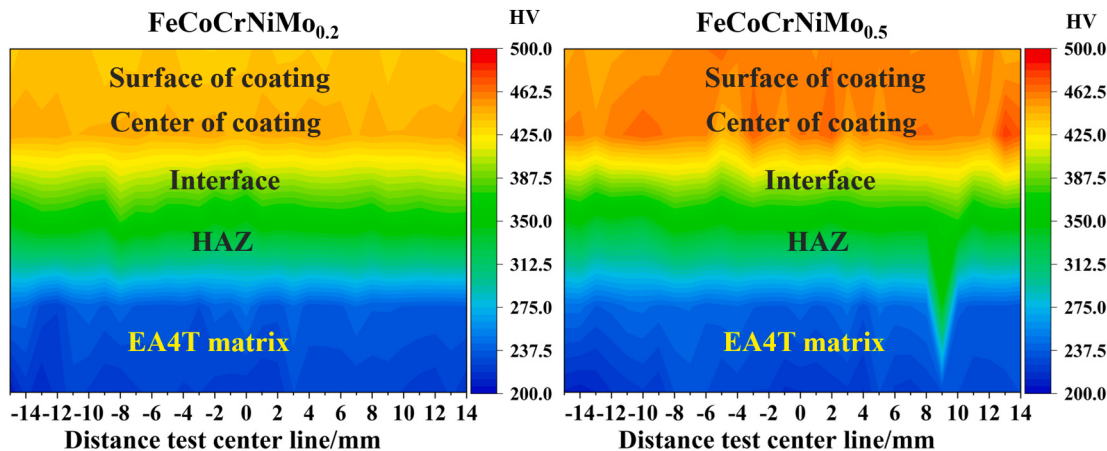


Fig. 7. Microhardness distribution of two HEAs coatings on cross sections: (a) FeCoCrNiMo_{0.2}; (b) FeCoCrNiMo_{0.5}.

observed that the boundaries of the four regions in the fracture surface of the FeCoCrNiMo_{0.2} sample are relatively clear. The fracture surfaces of the cladding layer and the heat-affected zone are relatively flat, dull, and without obvious metallic luster. In the matrix part, the fibrous region exhibits significant plastic deformation, with uneven fracture surfaces and strong light scattering ability, appearing dark gray. Radial patterns can be observed in the radiated region, with rough fracture surfaces and obvious metallic luster. The boundaries of the four regions in the fracture surface of the FeCoCrNiMo_{0.5} sample are also relatively clear. Some bright inclined surfaces appear in the cladding layer, which is caused by the increase of Mo content and the resulting increase in internal stress. The fracture surfaces of the heat-affected zone are also

relatively flat, dull, and without obvious metallic luster. The matrix part is similar to FeCoCrNiMo_{0.2}, with uneven fracture surfaces and a dark gray color. Radial patterns can be observed in the radiated region, with rough fracture surfaces and obvious metallic luster.

Comparative analysis of the cladding layer (Fig. 8 (f,g) and Fig. 10 (d, f)), bonding zone (Fig. 8 (b,d) and Fig. 10 (b,e)), heat-affected zone (Fig. 8 (c,e) and Fig. 10 (c)), and matrix section (Fig. 8 (h) and Fig. 10 (g, h)) of the two compositions of alloys reveals that the cladding layers of both HEAs show dense ductile dimples, indicating ductile fracture. The heat-affected zone and the bonding interface are mixed zones of two fracture mechanisms. The larger size of the primary coexisting ferrite in the matrix leads to a decrease in the plasticity and toughness of the

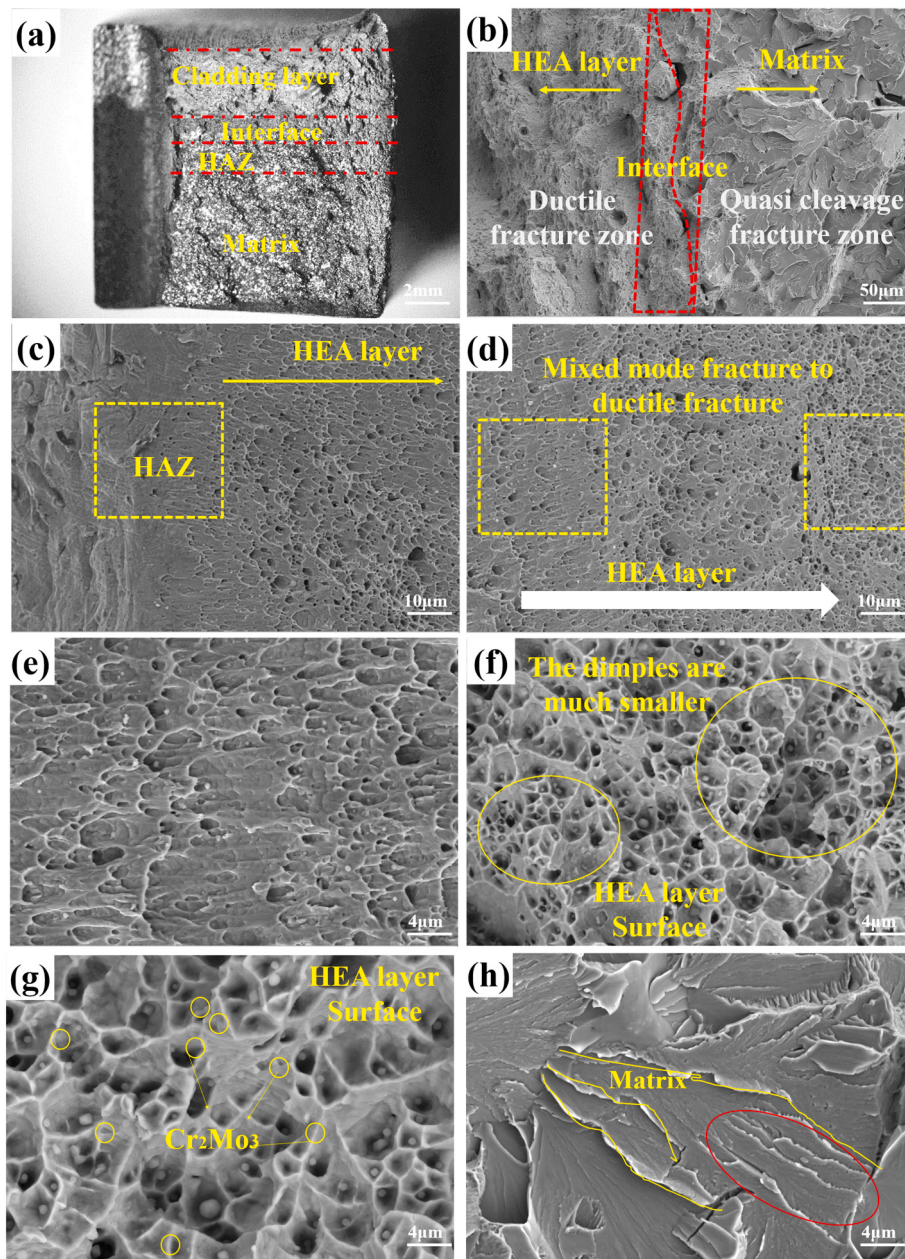


Fig. 8. Impact fracture morphology of FeCoCrNiMo_{0.2}: (a) Overall macroscopic morphology; (b, c, d) Binding zone; (e, f, g) Cladding layer; (h) Matrix.

ferrite, resulting in brittle fracture.

Both cladding layers contain fine dispersed metal intermetallic compounds such as Co₂Mo₃, CoMo₂Ni, Cr₉Mo₂₁Ni₂₀. Fig. 9 and Fig. 11 respectively show the EDS spectra of the coating fracture surface. It can be observed that the second-phase particles within the dimples are composed of Cr and Mo. These compounds hinder the movement of dislocations during crack propagation. When the moving dislocation lines pass through the intermetallic compound particles, dislocation loops are formed, resulting in the formation of microvoids. Due to the continuous accumulation of dislocations, the microvoids grow and form small ductile dimples. The ductile dimples in the FeCoCrNiMo_{0.2} cladding layer are smaller, indicating its stronger ability for plastic deformation, which can to some extent prevent crack propagation. With the increase of Mo content, the increase in intermetallic compounds leads to the presence of more hard and brittle phases in the material, and these phases usually have larger ductile dimple sizes. Since the formation of intermetallic compounds occurs at high temperatures, they often hinder

plastic deformation. In addition, in some cases, the increase of intermetallic compounds can also lead to the formation of larger agglomerates (such as grain-like structures) around some ductile dimples, thereby reducing the overall plasticity and toughness of the material. Therefore, although intermetallic compounds are beneficial for improving the strength and hardness of the material, their influence on the plasticity and toughness of the material needs to be considered in specific applications. EDS analysis revealed that the white particles were rich in Mo and identified as σ phase (Fig. 5, Fig. 6). This Mo-rich second phase increased the hardness of the coating to some extent [48,49], but reduced its toughness. FeCoCrNiMo_{0.5} exhibited higher dislocation density and more white particles, indicating higher hardness [50].

Meanwhile, combining the results of microstructure and hardness tests and analysis, it can be concluded that the decrease in impact toughness of FeCoCrNiMo_{0.5} is due to the combined effects of the content of intermetallic compounds, the density of dislocations, and the degree of oxidation.

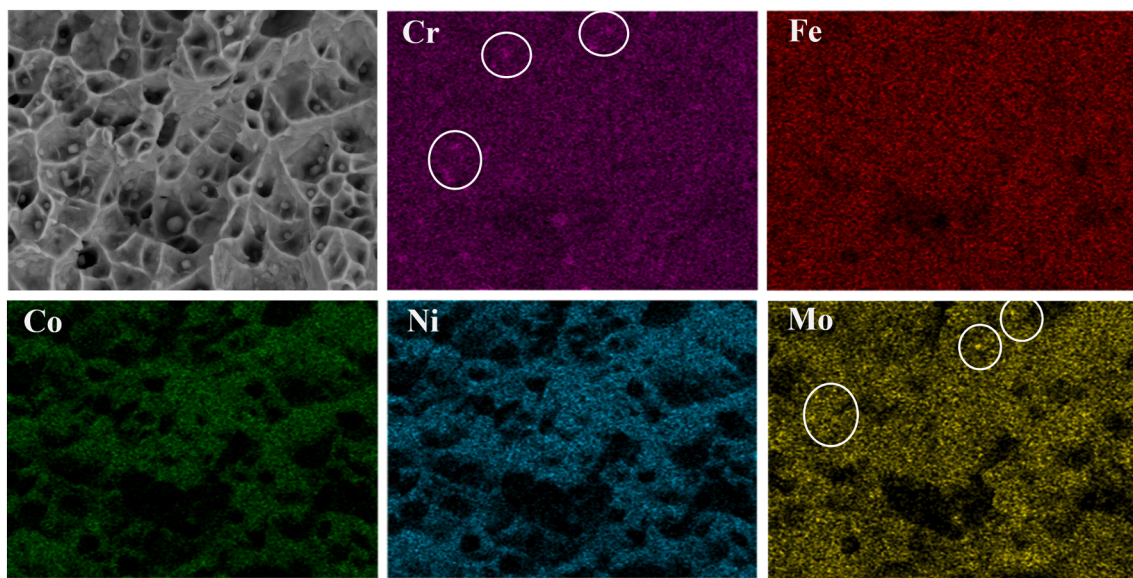


Fig. 9. EDS energy spectrum of FeCoCrNiMo_{0.2} coating surface (Fig. 8 (g)).

3.4. Calculation results

The structural models of FeCoCrNiMo_x ($x = 0.2, 0.5$) HEAs with two different compositions were calculated using first-principles calculations. The elastic stiffness constants C_{ij} at the equilibrium volume, as well as the bulk modulus (B), shear modulus (G), Young's modulus ϵ , Poisson's ratio (ν), and the elastic anisotropy of the structures were obtained. Fig. 12 (a,b) show that the lattice vectors undergo certain changes with the increasing Mo content, which affects the structural properties.

The ductility or brittleness of a material can be determined by the ratio of the bulk modulus to the shear modulus (B/G). When B/G > 1.75, the material is considered ductile, while when B/G < 1.75, the material is considered brittle. ν is also used to determine the ductility or brittleness of a material. Materials with a ν higher than 1/3 are ductile, while materials with a ν lower than 1/3 are brittle. Fig. 12(c) shows that both compositions of the materials are ductile. With the increase of Mo content, both B/G and ν values decrease, indicating a decrease in ductility. These data suggest that FeCoCrNiMo_{0.2} has higher plasticity and toughness compared to FeCoCrNiMo_{0.5}. Fig. 12(d) shows the anisotropy index A_U of the two materials. The A_U value of FeCoCrNiMo_{0.2} is 0.005, while the A_U value of FeCoCrNiMo_{0.5} is 0.085. A smaller A_U value indicates less elastic anisotropy, signifying a more uniform stress response in different directions. Conversely, a larger A_U value indicates greater elastic anisotropy, suggesting a larger difference in stress response in different directions.

Fig. 13(a) shows that the Poisson's ratio values of the two HEAs along the [100] crystal direction are 0.3851 (FeCoCrNiMo_{0.2}) and 0.3697 (FeCoCrNiMo_{0.5}). Fig. 13(b) shows that the intersection volume modulus values at the (001) crystal plane and the same crystal plane along the [100] crystal direction are 369.907 GPa (FeCoCrNiMo_{0.2}) and 272.543 GPa (FeCoCrNiMo_{0.5}). Fig. 13(c) shows that the projection curves of the Young's modulus exhibit irregular shapes (circular or square), and the Young's modulus values at the intersection points on the (001) crystal plane and the same crystal plane along the [100] crystal direction are 317.87 GPa (FeCoCrNiMo_{0.2}) and 212.92 GPa (FeCoCrNiMo_{0.5}). Fig. 13(d) shows that the shear modulus projection curves at the intersection points on the (001) crystal plane and the same crystal plane along the [100] crystal direction are 107.38 GPa (FeCoCrNiMo_{0.2}) and 101.36 GPa (FeCoCrNiMo_{0.5}).

The overall mechanical performance of FeCoCrNiMo_{0.2} is superior to FeCoCrNiMo_{0.5}, which is consistent with the mechanical performance

tests. This demonstrates the accuracy and advantages of first-principles calculations in the design and development of new alloys.

4. Conclusions

1. Using laser cladding technology, a coating with excellent metallurgical bonding, consisting of FeCoCrNiMo_x ($x = 0.2, 0.5$), is successfully prepared on the EA4T axle steel matrix. With the increase of Mo content, the degree of lattice distortion in the coating increased, and the diffraction peak shifted to the left. The increase in Mo content promoted the formation of σ phase and had the effect of refining the grain size. The degree of lattice distortion in the FeCoCrNiMo_{0.5} coating is greater, resulting in smaller grain size, providing important basis for the regulation of coating performance.

2. Both FeCoCrNiMo_{0.2} and FeCoCrNiMo_{0.5} coatings are composed of a cellular structure with high-density dislocations and Mo-rich σ phase particles. As the Mo content increased, the dislocation density and the quantity of σ phase increased, leading to an increase in the peak hardness of the coating from 456.5 HV to 469.4 HV, while the impact toughness decreased from 56 J to 16 J, indicating a competitive relationship between hardness and toughness.

3. The first-principle calculation results show that the B/G of the two coating materials are >1.75, and the ν is >1/3, indicating that both of them are ductile materials. However, with the increase of Mo content, the B/G and ν values decrease, the elastic anisotropy index A_U increases, and the plastic toughness deteriorates. The calculated results correspond well with the experimental results. It is indicated that the first principles calculation has reference value in the design and screening of coating components.

CRediT authorship contribution statement

Junjun Jin: Writing – review & editing, Writing – original draft, Validation, Investigation, Conceptualization. **Bing Chen:** Validation, Investigation. **Zhiyi Zhang:** Supervision, Project administration. **Yibin Wu:** Data curation. **Zhaoyang Luo:** Data curation. **Guoqing Gou:** Writing – review & editing, Project administration, Methodology, Funding acquisition. **Wenjing Chen:** Writing – review & editing, Writing – original draft, Data curation.

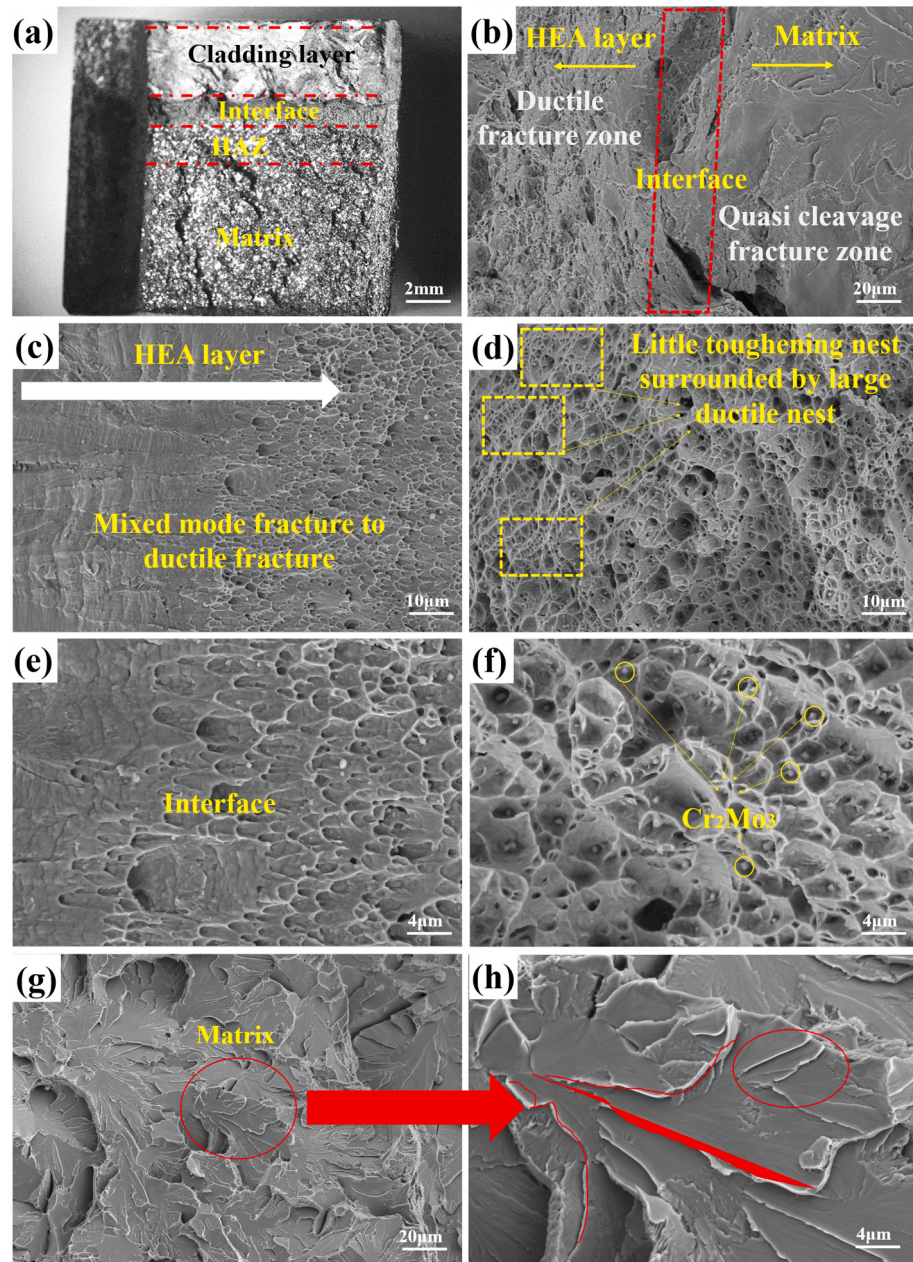


Fig. 10. Impact fracture morphology of FeCoCrNiMo_{0.5}: (a) Overall macroscopic morphology; (b, c, d) Binding zone; (e, f) Cladding layer; (g,h) Matrix.

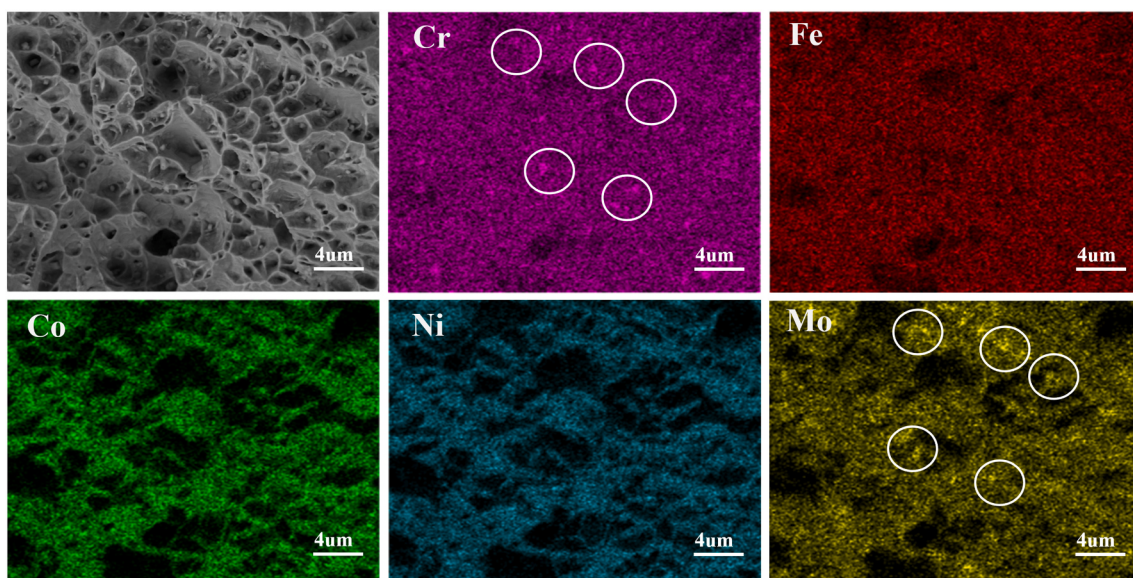


Fig. 11. EDS energy spectrum of FeCoCrNiMo_{0.5} coating surface (Fig. 10 (f)).

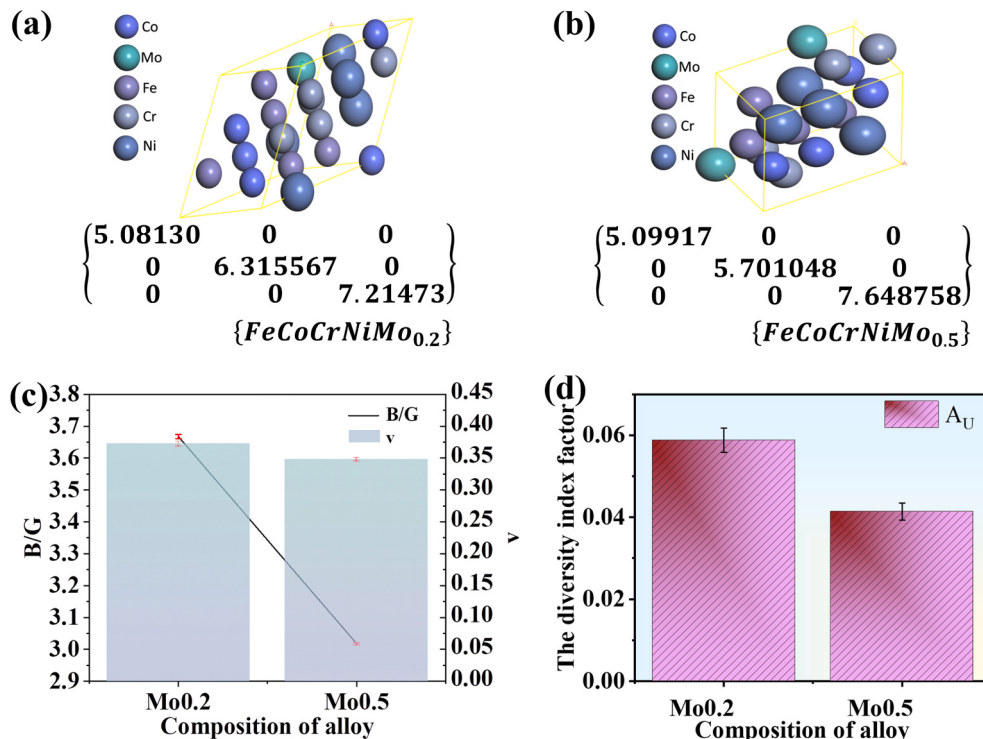


Fig. 12. First-principles calculation results: (a) Geometrically optimized model of FeCoCrNiMo_{0.2}; (b) Geometrically optimized model of FeCoCrNiMo_{0.5}; (c) B/G and Poisson's ratio of the two compositions; (d) Anisotropy index (A_U).

Declaration of competing interest

The authors declare that they have no known competing financial interests or personal relationships that could have appeared to influence the work reported in this paper. All authors of this manuscript have directly participated in planning, execution, and analysis of this study. The contents of this manuscript have not been copyrighted or published previously. The contents of this manuscript are not now under consideration for publication elsewhere. The contents of this manuscript will not be copyrighted, submitted, or published elsewhere while acceptance by Surface & Coatings Technology is under consideration. There are no

directly related manuscripts or abstracts, published or unpublished, by any authors of this manuscript. We declare that we do not have any commercial or associative interest that represents a conflict of interest in connection with the work submitted.

Data availability

Data will be made available on request.

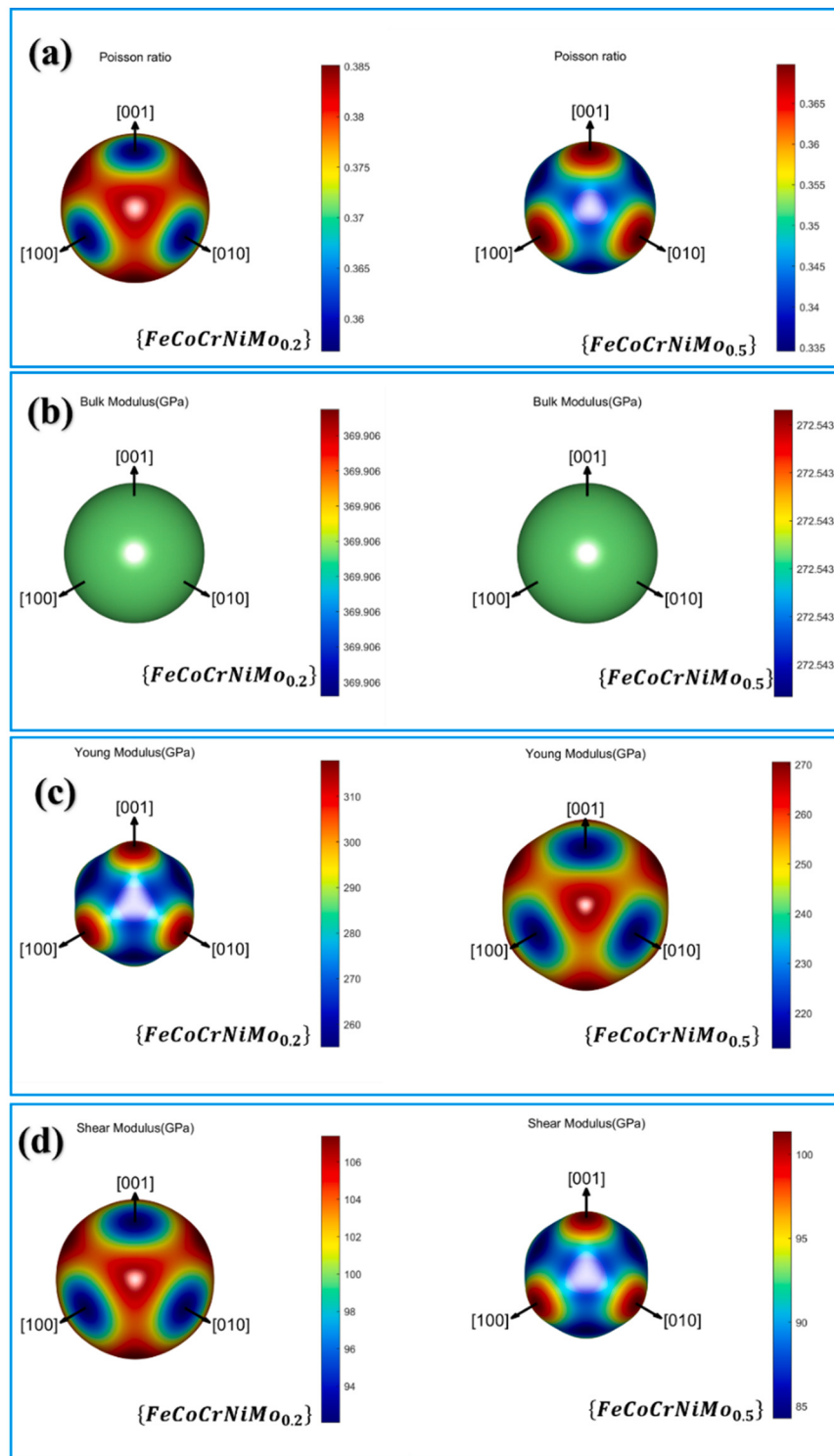


Fig. 13. 3D surface plots of the anisotropy of two HEAs: (a) Poisson's ratio (ν), (b) Bulk modulus (B), (c) Young's modulus (E), (d) Shear modulus (G).

Acknowledgements

This research did not receive any specific grant from funding agencies in the public, commercial, or not-for-profit sectors.

References

- [1] J. Gao, et al., Failure causes and hardening techniques of railway axles – a review from the perspective of structural integrity, Eng. Fail. Anal. 141 (2022) 106656.

- [2] H. Li, et al., Corrosion fatigue mechanism and life prediction of railway axle EA4T steel exposed to artificial rainwater, Eng. Fail. Anal. 138 (2022) 138.
- [3] A. Bevan, et al., Development and validation of a wheel wear and rolling contact fatigue damage model, Wear 307 (1–2) (2013) 100–111.
- [4] D. Hou, et al., High-speed train wheel set bearing fault diagnosis and prognostics: research on acoustic emission detection mechanism, Mech. Syst. Signal Process. (2022) 179.
- [5] O.A. Waseem, et al., The effect of Ti on the sintering and mechanical properties of refractory high-entropy alloy $Ti_xW_{1-x}Cr$ fabricated via spark plasma sintering for fusion plasma-facing materials, Mater. Chem. Phys. 210 (2018) 87–94.

- [6] Q. Xiao, et al., Wear mechanisms and micro-evaluation on WC particles investigation of WC-Fe composite coatings fabricated by laser cladding, *Surf. Coat. Technol.* 420 (9) (2021) 127341.
- [7] S. Zhang, et al., Microstructure and anodic electrochemical behavior of additive manufactured Hastelloy X alloy via directed energy deposition, *Addit. Manuf.* 39 (2021) 101824.
- [8] C. Bai, et al., Microstructure evolution and cyclic deformation behavior of Ti-6Al-4 V alloy via electron beam melting during low cycle fatigue, *Int. J. Fatigue* 159 (2022) 106784.
- [9] I. Hemmati, V. Ocelik, J. Hosson, Dilution effects in laser cladding of Ni-Cr-B-Si-C hardfacing alloys, *Mater. Lett.* 84 (2012) 69–72.
- [10] S. Zhou, et al., Effect of laser remelting on microstructure and properties of WC reinforced Fe-based amorphous composite coatings by laser cladding, *Opt. Laser Technol.* 103 (2018) 8–16.
- [11] W. Gao, et al., Effect of re-melting on the cladding coating of Fe-based composite powder, *Mater. Des.* 64 (2014) 490–496.
- [12] A. Sharma, High entropy alloy coatings and technology, *Coatings* 11 (4) (2021) 372.
- [13] Junbo, et al., The effects of heat treatment on microstructure and mechanical properties of Tribaloy 400 coatings deposited by laser cladding, *J. Mater. Eng. Perform.* 27 (2018) 6339–6348.
- [14] Z. Zhu, et al., Effects of Cu/Si on the microstructure and tribological properties of FeCoCrNi high entropy alloy coating by laser cladding, *Wear* 512-513 (2023) 204533.
- [15] J. Hu, X. Lin, Y. Hu, High wear resistance and strength of Hastelloy X reinforced with TiC fabricated by laser powder bed fusion additive manufacturing, *Appl. Surf. Sci.* 648 (2024) 159004.
- [16] Z. Zhang, et al., Influence of heat treatment on microstructures and mechanical properties of K447A cladding layers obtained by laser solid forming, *Journal of Alloys & Compounds* 790 (2019) 703–715.
- [17] A. Bartkowski, Laser Cladding Process of Fe/WC Metal Matrix Composite Coatings on Low Carbon Steel Using Yb: YAG Disk Laser 136(1), *Optics & Laser Technology*, 2021.
- [18] H. Song, et al., Laser melting deposition of K403 superalloy: the influence of processing parameters on the microstructure and wear performance, *J. Alloys Compd.* 805 (2019) 551–564.
- [19] J.W. Yeh, et al., Nanostructured high-entropy alloys with multiple principal elements: novel alloy design concepts and outcomes, *Adv. Eng. Mater.* 6 (2004).
- [20] J. Li, et al., Tuning the mechanical behavior of high-entropy alloys via controlling cooling rates, *Materials Science & Engineering, A. Structural Materials: Properties, Microstructure and Processing* 760 (2019) 760.
- [21] L. Jia, et al., Transformation induced softening and plasticity in high entropy alloys, *Acta Mater.* 147 (2018) 35–41.
- [22] J.W. Yeh, et al., Nanostructured high-entropy alloys with multiple principal elements: novel alloy design concepts and outcomes, *Adv. Eng. Mater.* 6 (5) (2004) 299–303.
- [23] L. Huang, et al., Microstructure characteristics and mechanical behaviour of a selective laser melted Inconel 718 alloy, *J. Mater. Res. Technol.* 9 (2) (2020).
- [24] Q. Fang, et al., Probing the phase transformation and dislocation evolution in dual-phase high-entropy alloys, *Int. J. Plast.* 114 (2019) 161–173.
- [25] B. Cai, et al., Deformation mechanisms of Mo alloyed FeCoCrNi high entropy alloy: in situ neutron diffraction, *Acta Mater.* 127 (2017) 471–480.
- [26] K. SW, Y. JW, C. TS, Rapidly solidified structure of alloys with up to eight equal-molar elements - a simulation by molecular dynamics, *J. Phys. Condens. Matter* 20 (14) (2008).
- [27] G.G. Kresse, J.J. Furthmüller, Efficient iterative schemes for ab initio total-energy calculations using a plane-wave basis set, *Phys. Rev. B Condens. Matter* 54 (1996) 11169.
- [28] Y. Cai, et al., A review of in-situ monitoring and process control system in metal-based laser additive manufacturing, *J. Manuf. Syst.* 70 (2023) 309–326.
- [29] M. Ma, et al., Modeling and optimization for laser cladding via multi-objective quantum-behaved particle swarm optimization algorithm, *Surf. Coat. Technol.* 381 (2020) 125129.
- [30] X. Zeng, et al., Microstructure and high-temperature properties of laser cladded AlCoCrFeNiTi0.5 high-entropy coating on Ti 6Al-4V alloy, *Surf. Coat. Technol.* 418 (2021) 127243.
- [31] L. Zhai, et al., Characteristics of dilution and microstructure in laser cladding Ni-Cr-B-Si coating assisted by electromagnetic compound field, *Mater. Lett.* 243 (2019) 195–198.
- [32] Y. Fu, et al., Evolution in microstructure, wear, corrosion, and tribocorrosion behavior of Mo-containing high-entropy alloy coatings fabricated by laser cladding, *Corros. Sci.* 191 (2021) 109727.
- [33] R. Li, et al., Dilution effect on the formation of amorphous phase in the laser cladded Ni-Fe-B-Si-Nb coatings after laser remelting process, *Appl. Surf. Sci.* 258 (20) (2012) 7956–7961.
- [34] Standardization Administration of the People's Republic of China, GB/T229-2020, Standard for Charpy Pendulum Impact Test Methods for Metallic Materials, 2020.
- [35] L. Jiang, et al., Effect of Mo and Ni elements on microstructure evolution and mechanical properties of the CoFeNiXMo high entropy alloys, *J. Alloys Compd.* 649 (2015) 585–590.
- [36] W. Zhao, et al., Al and Mo synergistic enhancement of CoCrFeNi high-entropy alloy laser cladding layer, *J. Mater. Res. Technol.* 28 (2024) 2572–2581.
- [37] S. Yan, et al., The effect of multi-element alloying on the structure and properties of laser cladding nickel-based coatings, *Surf. Coat. Technol.* 454 (2023) 129174.
- [38] X. Liu, et al., Microstructure and corrosion property of TC4 coating with Al0.5CoCrFeNi high-entropy alloy interlayer by laser cladding, *Surf. Coat. Technol.* 476 (2024) 130190.
- [39] D. Kong, et al., About metastable cellular structure in additively manufactured austenitic stainless steels, *Addit. Manuf.* 38 (2021) 101804.
- [40] Z. Fu, et al., Hydrogen-assisted fatigue crack propagation behavior of selective laser-melted Inconel 718 alloy, *Corros. Sci.* 227 (2024) 111745.
- [41] P. Liu, et al., Microstructural evolution and phase transformation of Inconel 718 alloys fabricated by selective laser melting under different heat treatment, *J. Manuf. Process.* 39 (2019) 226–232.
- [42] L. Huang, et al., Microstructure characteristics and mechanical behaviour of a selective laser melted Inconel 718 alloy, *J. Mater. Res. Technol.* 9 (2) (2020) 2440–2454.
- [43] A.R. Balachandramurthy, et al., Microstructural influence on fatigue crack propagation during high cycle fatigue testing of additively manufactured Alloy 718, *Mater. Charact.* 149 (2019) 82–94.
- [44] X. Zhang, et al., Corrosion behaviour of CoCrMo alloys in 2 wt% sulphuric acid solution, *Electrochim. Acta* 125 (2014) 543–555.
- [45] J. Miao, et al., Optimization of mechanical and tribological properties of FCC CrCoNi multi-principal element alloy with Mo addition, *Vacuum* 149 (2018) 324–330.
- [46] H. Liu, et al., Microstructure and high-temperature wear behavior of CoCrFeNiWx high-entropy alloy coatings fabricated by laser cladding, *Tribol. Int.* 172 (2022) 107574.
- [47] J. Wang, et al., Investigation of the micromechanical behavior of a Ti68Nb7Ta3Zr4Mo18 (at.%) high-entropy alloy, *Materials* 16 (14) (2023) 5126.
- [48] X. Wen, et al., Novel nano-lamellar AlCoCrFeMn0.5Mo0.1Nb_x eutectic high-entropy alloy coatings by ultrasonic assisted laser cladding: microstructure and tribological behaviors, *Intermetallics* 156 (2023) 107851.
- [49] X. Wen, et al., Design and characterization of FeCrCoAlMn0.5Mo0.1 high-entropy alloy coating by ultrasonic assisted laser cladding, *J. Alloys Compd.* 835 (2020) 155449.
- [50] X. Wen, et al., Corrosion and tribocorrosion behaviors of nano-lamellar Ni1.5CrCoFe0.5Mo0.1Nb_x eutectic high-entropy alloy coatings: the role of dual-phase microstructure, *Corros. Sci.* 201 (2022) 110305.